

Contents lists available at ScienceDirect

# Journal of Membrane Science

journal homepage: www.elsevier.com/locate/memsci





# Phase-field modeling of non-solvent induced phase separation (NIPS) for PES/NMP/Water with comparison to experiments

M. Rosario Cervellere <sup>a</sup>, Xianghong Qian <sup>b</sup>, David M. Ford <sup>c</sup>, Christina Carbrello <sup>d</sup>, Sal Giglia <sup>d</sup>, Paul C. Millett <sup>a,\*</sup>

- <sup>a</sup> University of Arkansas, Department of Mechanical Engineering, Fayetteville Arkansas, 72701, USA
- b University of Arkansas, Department of Biomedical Engineering, Fayetteville Arkansas, 72701, USA
- <sup>c</sup> University of Arkansas, Ralph E. Martin Department of Chemical Engineering, Fayetteville Arkansas, 72701, USA
- d MilliporeSigma, 80 Ashby Road, Bedford Massachusetts, 01730, USA

# ARTICLE INFO

# Keywords: Solvent-induced phase separation Phase-field modeling Computer simulation Polymer membrane

#### ABSTRACT

We develop a phase-field model to simulate the formation of porous polymeric membranes via non-solvent induced phase separation. The material system of interest is PES/NMP/Water (Polyethersulfone/N-methyl-2-pyrrolidone/Water), however the approach is broadly applicable to other materials. The three-component system is represented with two field variables: one representing the volume fraction of polymer, and the other the fractional composition of non-solvent N (water) vs solvent S (NMP). The exchange of solvent and non-solvent is solved with a Fickian diffusion model, thus capturing the in-flux of the coagulation bath into the polymer solution. As a demonstration of the predictive capabilities of the model, the concentration of solvent (NMP) in the coagulation bath was varied to draw comparisons with experiments. Two- and three-dimensional simulations were carried out to evaluate the cross-sectional pore morphology and the top surface pore size for membranes formed by NIPS. Experiments involving handcast membranes of a similar system were performed for comparison with the simulations, and an agreement was found concerning the dependence of pore morphology on the composition of the coagulation bath.

# 1. Introduction

One of the primary methods for fabricating flat-sheet membrane filters involves non-solvent induced phase separation (NIPS), whereby a polymer solution is exposed to a coagulation bath containing a non-solvent (otherwise known as a poor solvent) and the polymer precipitates out of solution resulting in a porous network [1–4]. A depiction of the NIPS process is shown in Fig. 1. The mechanisms pertaining to the formation of specific morphologies and defects are complex and mostly explained by heuristic knowledge of experimental process conditions.

Computational modeling of the membrane formation process is a developing branch of research with the aim to accelerate industrial R&D, aid in tailoring membrane performance, and assist in developing new membranes from novel materials. The large number of process control variables, cost of experimental exploration, and time-consuming research and development are primary motivations for computational research in an effort to understanding *in-situ* phenomenon and predict membrane morphologies. Different modeling techniques have been applied to this specific problem and include molecular-scale simulations, mesoscale simulations, and macroscale simulations.

Molecular-scale simulations are capable of predicting polymer chain behavior during phase inversion; however, the length scales are in the range of tens of nanometers which is at least one order of magnitude smaller than a full membrane thickness. Dissipative particle dynamics (DPD) have been widely utilized and can predict solution behavior during phase separation at nanoscale dimensions (up to 100-200 nm). Work done by Wang et al. [5] investigated the basics of NIPS in two dimensions by observing the exchange of non-solvent (into the polymer solution) and solvent (out of the polymer solution) and the resulting phase separation process. The kinetics of phase inversion have also been characterized with DPD simulations with relationships drawn to the mesoscale [6]. The effect of additives on membrane morphology studied by Tang et al. [7] show how the strength of interactions for the additive and other components can have a significant effect on membrane structure. Further work by Tang et al. [8-10] extended the previous work into three dimensions and incorporated mass transfer at the coagulation bath interface with a focus on the formation of a dense pore layer at this interface. This work has been expanded upon to understand how the strength of interaction between

E-mail address: pmillett@uark.edu (P.C. Millett).

<sup>\*</sup> Corresponding author.

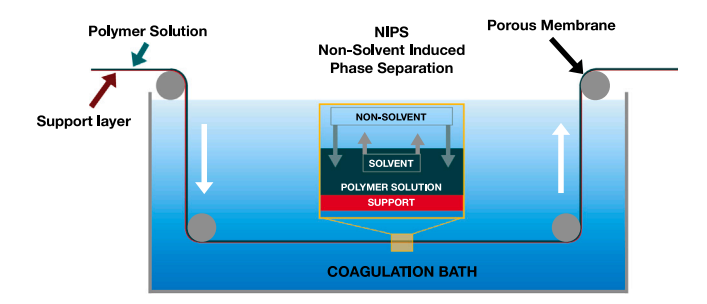


Fig. 1. Schematic of the NIPS membrane formation process.

non-solvent and solvent affect the rate of phase separation and the resulting morphology [11].

Modeling work that has been carried out in the mesoscale using the phase-field (PF) method is proving capable of capturing pore morphologies and domain sizes closer to the thickness of a filtration membrane. One-dimensional simulations by Caneba et al. [12] used the Cahn-Hilliard equation with the Flory-Huggins (FH) free energy of mixing to investigate the formation of anisotropic membrane structures. Twodimensional simulations by Barton et al. [13,14] investigated the thermodynamic and transport properties of phase separation. The principal findings show that increasing polymer concentration slows the diffusive process of phase inversion during thermally induced phase separation (TIPS). Two dimensional simulations carried out by Fernandes et al. [15] explored a simplified model in order to reduce the number of parameters needed for simulations. The principal findings from the study include morphological changes to the dense pore region when adding solvent to the coagulation bath, adding non-solvent to the polymer solution, and the effect of membrane thickness on the initial casting solution.

Two and three-dimensional simulations coupled to the Navier-Stokes equation by Zhou et al. [16] also found the development of a dense pore region and characterized the effect of polymer concentration in the casting solution. Hopp-Hirschler and Nieken [17] conducted two-dimensional simulations with an imposed moving precipitation front, the velocity of which affected the morphology of pores. Two and three dimensional simulations carried out by Tree et al. [18-20] explored coarsening kinetics, Marangoni flows, and the inclusion of mass transfer and their effects on final morphology. Three dimensional TIPS simulations carried out by Mino et al. [21] looked at the late-stage morphological development of spinodal decomposition and how it was affected by early-stage morphology. Cervellere et al. [22] conducted three dimensional simulations of TIPS and found that the coagulation bath temperature and polymer concentration has a large effect on the depth of the dense pore region and the overall pore size, with higher coagulation bath temperatures and lower polymer concentrations favoring larger pores.

The Lattice-Boltzmann method has also been used recently to study the formation of anisotropic membrane structures [23]. Work done by Gan et al. [24,25] evaluated the role of component viscosities during TIPS, showing that the velocities of local flow were found to be inversely proportional to temperature, exemplifying the connection to casting temperature and morphology. Further work done by Gan et al. [26] included surface tension effects for the system thermodynamics and found two domains of phase separation — spinodal decomposition and nucleation/growth — however more work needs to be done to fully understand the coarsening kinetics.

The NIPS process has been studied by computational researchers in efforts to verify various models with experimental observations; however, a knowledge gap still exists relating to the formation of a dense skin layer as well as the origin of macrovoid formation. The Monte Carlo method was used by He et al. [27] and found that

the diffusion of non-solvent from the coagulation bath is exponentially decreased by the presence of polymer. It was also found that spinodal decomposition and nucleation/growth both occurred at different depths within the simulated membrane structure. The work done by Tree et al. [19] (mentioned previously) examined the effect of Marangoni flows on membrane formation however the results were inconclusive and showed the need for a method of implementing polymer vitrification, which was not included.

In this paper, we utilize a PF model to conduct both 2D and 3D simulations of the NIPS process in the specific material system of PES/NMP/water. Here, we specifically investigate the effect of independently varying two key parameters: the polymer volume fraction in solution and the coagulation bath composition. In addition, a model to capture vitrification of the polymer-rich phase has been implemented and found to satisfactorily halt coarsening in regions with high polymer content. Combining this mesoscale model with modern high-performance computing enables large simulation domains in the micrometer scale that allow direct comparisons with scanning-electron microscope images. The NIPS simulations are evaluated by observing the cross-sectional and top-surface morphology given different casting conditions. The simulations are then compared to handcast membranes produced with similar casting conditions.

# 2. Methods

Our PF model evolves two field variables that together sufficiently describe the three-component systems typical of NIPS processing. The first field variable represents the polymer volume fraction,  $\phi_P$ . The two remaining components (water and NMP) are both small-molecule solvents that are fully miscible with one another. Therefore, we treat the solvent as a two-component mixture, and the compositional fraction of which is represented by  $f_N$  whereby N signifies non-solvent which in this case corresponds to water. As there are exactly two solvents, one can tacitly determine the amount of NMP as  $1-f_N$ . The polymer volume fraction is evolved with a Cahn–Hilliard–Cook equation [28]:

$$\frac{\partial \phi_P}{\partial t} = \nabla \cdot \left( M_P \nabla \left( \frac{\delta F_{mix}}{\delta \phi_P} - 2\kappa \nabla^2 \phi_P \right) \right) + \xi, \tag{1}$$

where  $M_P$  is the polymer mobility,  $F_{mix}$  is the free energy of mixing,  $\kappa$  scales the interfacial energy between the two phases, and  $\xi$  is a random number centered at zero that imparts a small thermal fluctuation to the polymer concentration. The polymer mobility is related to the polymer diffusivity by the equation [16]:

$$M_P = \frac{D_P}{\partial^2 F_{mix} / \partial \phi_P^2} \tag{2}$$

where  $D_P$  is the diffusion coefficient of a polymer chain in solution.

The binary FH free energy of mixing used in this work is given below [29]:

$$F_{mix} = k_b T \left[ \frac{\phi_P}{N} \ln \phi_P + \phi_S \ln \phi_S + \chi \phi_P \phi_S \right], \tag{3}$$

where the substitution  $\phi_S=1-\phi_P$  is made for the solvent. The degree of polymerization is N=150, the temperature is 298 K (25 °C), and  $\chi$  is the interaction parameter between polymer and solvent. This interaction parameter determines miscibility between polymer and solvent and can be dependent on temperature, composition, or a combination of process conditions that are prevalent during casting. In this work, we assume isothermal conditions and therefore  $\chi$  depends solely on composition with the below weighted average:

$$\chi = f_N \chi_{PN} + (1 - f_N) \chi_{PS},\tag{4}$$

where  $\chi_{PN}=1.5$  is the interaction parameter between PES and water and  $\chi_{PS}=0.034$  is the interaction parameter between PES and NMP, both values set for T=25 °C [30–32]. As the local non-solvent fraction increases,  $\chi$  also increases and can ultimately surpass the critical value that in turn activates phase separation. The FH free energy of mixing

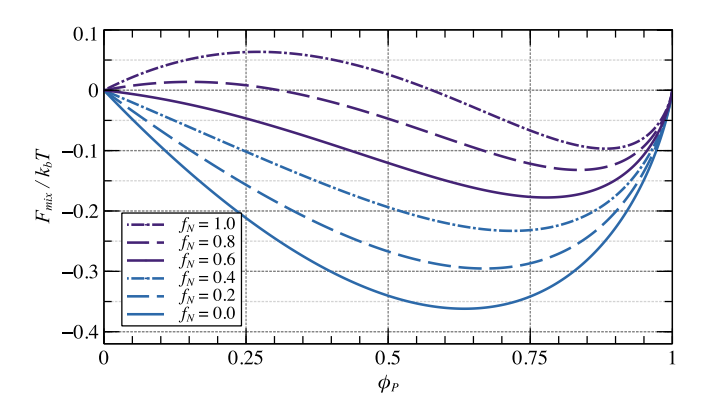


Fig. 2. Free energy of mixing for six different non-solvent fractions  $f_N$  calculated from Eqs. (3) and (4). As  $f_N$  increases, the polymer solution goes from miscible to immiscible

is directly affected by the presence of non-solvent as depicted Fig. 2 where the FH free energy is plotted for a range of  $f_N$ .

We assume that the exchange of solvents between the polymer solution and the coagulation bath (water into and NMP out of the polymer solution) is a diffusion-governed process, and we use a Fickian diffusion model to evolve  $f_N$ . Therefore, in the current implementation, we ignore hydrodynamic transport, although that can be added in the future. The evolution equation is written as:

$$\frac{\partial f_N}{\partial t} = \nabla \cdot \left( D_N(\phi_P) \nabla f_N \right),\tag{5}$$

where  $D_N$  represents the diffusivity of the non-solvent species, and it is dependent of the local value of  $\phi_P$  hence it is spatially heterogeneous.

The diffusivity of polymer in solution is described with the Phillies model [33,34]:

$$D_P = D_P^o exp(-\alpha c^{\nu}) \tag{6}$$

where the pre-exponential  $D_P^o$  is the diffusion coefficient of a single polymer chain in solution (the dilute limit),  $\alpha$  and  $\nu$  are scaling coefficients to fit experimental data, and c is the mass concentration of polymer with units of g/L. This mass concentration is calculated from  $\phi_P$  according to  $c = \phi_P(M_w/M_{vol})$ , where  $M_w = 232.36$  g/mol and  $M_{vol} = 0.1683$  L/mol for PES. The scaling coefficients are assigned values of  $\alpha = 0.1$  and  $\nu = 0.6$  to achieve a similarly shaped diffusion curve that has been reported for PES in NMP [30]. After converting diffusivity to mobility (Eq. (2)) the mobility was scaled by a factor of 0.35 to achieve the same magnitude as the mobility derived from experimental diffusivity data previously reported [30].

Eq. (6) can describe general concentration-dependent diffusion and in this work was also used to calculate  $D_N$ :

$$D_N = D_N^o exp(-\alpha c^{\nu}) \tag{7}$$

where the pre-exponential  $D_N^o$  is the diffusion coefficient of a water molecule in the absence of polymer. The scaling coefficients for non-solvent diffusion were  $\alpha=0.2$  and  $\nu=0.4$  which allow for more rapid diffusion of non-solvent while reducing the concentration dependence for  $D_N$  in comparison to  $D_P$  [30]. The value of  $D_N^o$  was set an order of magnitude higher than that of  $D_P^o$  accounting for more rapid diffusion of water molecules as compared to polymer chains. Here,  $D_N^o=10^{-5}$  cm<sup>2</sup>/s and  $D_P^o=10^{-6}$  cm<sup>2</sup>/s which is similar to what has been reported in the literature [30,35]. The diffusion curves for polymer and non-solvent are shown in Fig. 3.

A cutoff volume fraction,  $\phi_{cutoff}$ , was used to vitrify the polymer domain in effect freezing the polymer-rich structures after phase separation. Once the polymer volume fraction exceeds a threshold,  $\phi_P \geq \phi_{cutoff}$ , the mobility is drastically reduced by dividing the mobility by a factor of  $10^6$ , vitrifying the polymer domain. This study

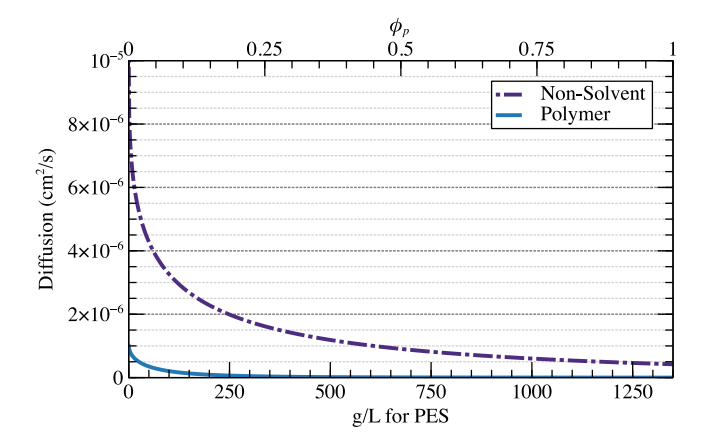


**Fig. 3.** Diffusivities for both polymer (PES) and water (non-solvent) calculated from Eq. (6). The diffusivities for both species decrease with increasing polymer content. The top x-axis represents the non-solvent concentration and the bottom x-axis represents the PES concentration.

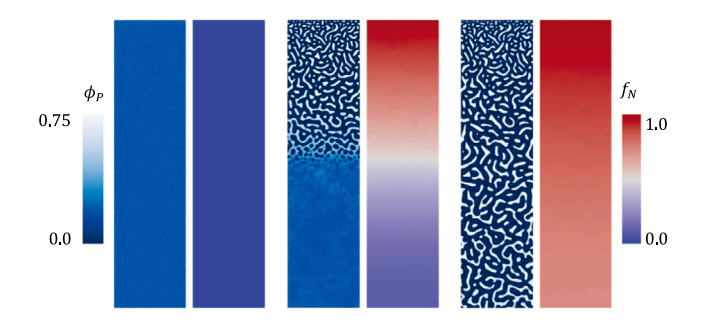


**Fig. 4.** Snapshots of a 2D simulation at times 0s (left), 0.735s (middle), and 2.205s (right). The fields of  $\phi_P$  and  $f_N$  for each time are shown side-by-side. The top surface maintains a constant value of  $f_N^{CB} = 1.0$ , and as non-solvent diffuses into the domain, phase separation occurs from top to bottom. Here, the average polymer volume fraction is  $\hat{\phi}_P = 0.2$ . The vitrification model freezes polymer-rich domains when  $\phi_P > 0.75$ .

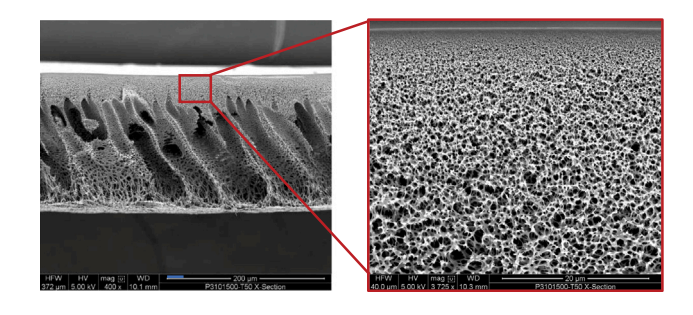


Fig. 5. Two SEM images showing the approximate scale of the simulations for drawing comparisons. The left image is the whole membrane cross section and the right image is a closer view corresponding to the scale of the simulations. The scale bar on the left image is 200  $\mu m$  and the scale bar on the right image is 20  $\mu m$ .

uses a cutoff volume fraction of  $\phi_{cutoff} = 0.75$  similar to polymer vitrification concentrations experimentally observed by Kim et al. [36]. All simulations below were run until complete vitrification occurred throughout the simulation domain.

To execute the simulations, Eqs. (1) and (5) are solved with an explicit finite difference scheme on a rectilinear grid with uniform spacing. To reduce round-off error, the equations are solved in reduced units of length ( $\bar{l}$ ) and time ( $\bar{l}$ ). The grid spacing  $\Delta x = 1$   $\bar{l}$ , the time step size is  $\Delta t = 0.01$   $\bar{t}$ , and  $D_P^o$  is set to unity (and hence  $D_N^o$  is set to 10). Following the simulations, the time and length scales are converted into physical units by assuming  $\bar{l} = 35$  nm (i.e. each grid node represents a box with side lengths of 35 nm) and  $\bar{t} = \bar{l}^2/(10^{-6} \text{cm}^2/\text{s}) = 10^{-6} \text{cm}^2/\text{s}$ 

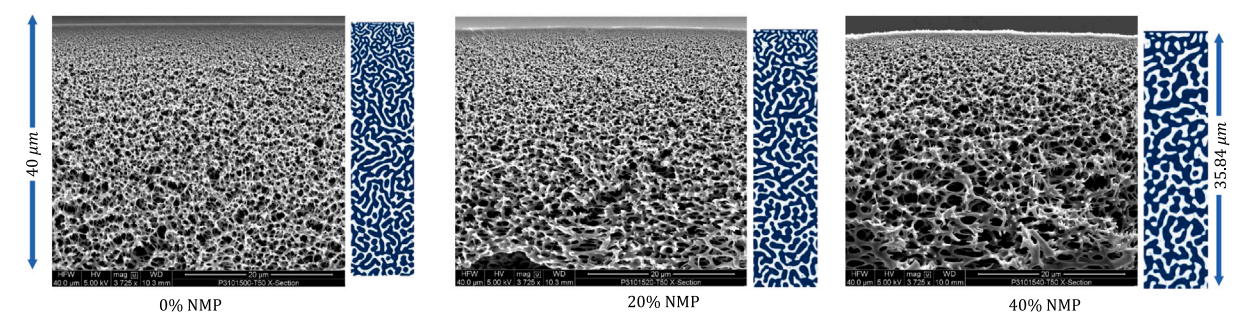
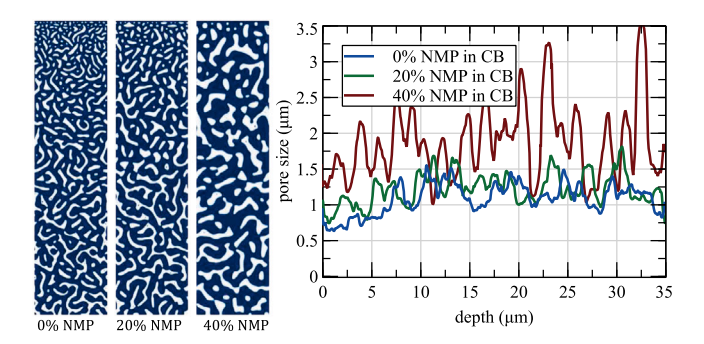
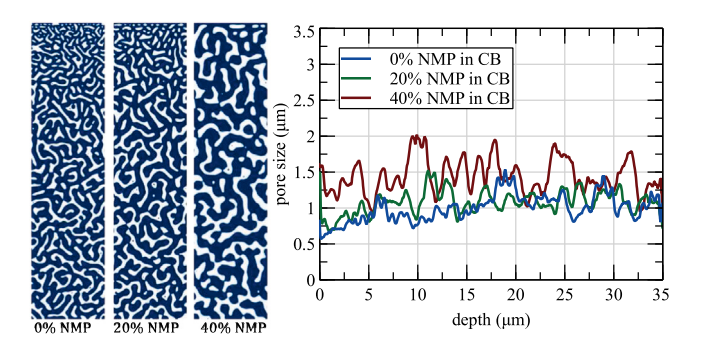


Fig. 6. Cross-sectional comparison between handcast membranes and simulations. From left to right the coagulation bath contained 0, 20, and 40 vol% NMP ( $f_N^{CB} = 1.0, 0.8$  and 0.6). The simulations show good qualitative agreement with experiments, both exhibiting anisotropic pore structures that increases in size as NMP is added to the coagulation bath. Here, the simulations have a  $\bar{\phi}_P = 0.25$ .



**Fig. 7.** (left) Final structures from three different 2D simulations with different coagulation bath compositions (as indicated), each with  $\bar{\phi}_P = 0.2$ . (right) Pore size versus membrane depth for the three coagulation bath compositions. As NMP is added to the coagulation bath the pore size at the top surface increases along with the pore size throughout the membrane structure.



**Fig. 8.** Same as Fig. 7, but with a polymer volume fraction of  $\bar{\phi}_P = 0.225$ .

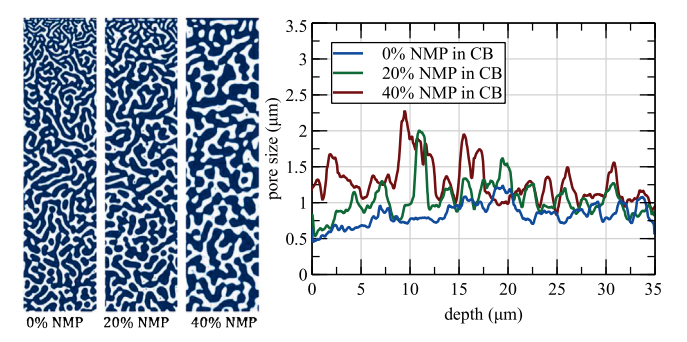


**Fig. 9.** Same as Fig. 7, but with a polymer volume fraction of  $\bar{\phi}_P = 0.25$ .

 $1.225\times10^{-5}$  ms. These values were chosen to allow for a simulation time window of 10 s and pore sizes in the micro-filtration range. In Eq. (1), the thermal fluctuation term  $\xi$  is a random number uniformly chosen

within the bounds [-0.05,0.05], and the interfacial energy term  $\kappa$  is set to unity. Setting  $\kappa$  to unity in conjunction with a grid spacing  $\Delta x = 1$   $\bar{l}$  resolves the interface width to 3–7 grid points. Adjusting  $\kappa$  results in a change in the interface energy and width, which would require simultaneous adjustment of  $\Delta x$ . We leave that for a future study.

The simulation domain has periodic boundary conditions imposed in the x- and y-directions with no-flux boundary conditions in the z-direction. Two-dimensional simulations exist in the xz-plane. The simulations are initialized with small fluctuations in  $\phi_P$  about the mean value  $\bar{\phi}_p$ , and  $f_N = 0$  inside the domain. The top surface in the zdirection represents the interface between the polymer solution and the coagulation bath. On this top surface, we assign a fixed value of  $f_N$ , which we denote as  $f_N^{\it CB}$ , that is constant in time and imposes a timedependent gradient of non-solvent within the domain thereby driving non-solvent diffusion into the polymer solution. This study looks at the effect of adding NMP to the coagulation bath, and we consider three different coagulation bath compositions  $f_N^{CB} = 1.0$ , 0.8, and 0.6, which correspond to 100% water, 80% water/ 20% NMP, and 60% water/40% NMP, respectively. Fig. 4 illustrates the co-evolution of  $\phi_P$ and  $f_N$  in a two-dimensional simulation of the NIPS process. Although it is not shown, we have observed that the presence of the polymerrich domains significantly slows down the in-flux of water due to the reduction of  $D_N$  in those regions. See Supplemental Movie 1 for an animation of Fig. 4.

Handcast membranes were prepared for morphological comparison to simulations. The recipe for the membrane was 15 wt% BASF PES E3010, 10 wt% PVP k90 (to increase solution viscosity and suppress macrovoids) and NMP. The polymer solution was mixed at 50 °C for at least 24 h. The polymer solution was then cast onto a plastic film taped to a glass pane heated to a temperature of 50 °C. The casted film was then inserted into the coagulation bath which was held at 50 °C and consisted of DI water and different vol% NMP (0%, 20%, and 40%). The membrane was then removed from the coagulation bath and soaked in DI water for 24 h before drying. The scale of the simulations and the region of interest for cross section comparisons are detailed in Fig. 5, where the top 40  $\mu m$  above the macrovoids are considered.

Current simulation methods are unable to capture the formation of macrovoids and accordingly the model presented simulates the formation of an idealized membrane structure free of macrovoids. Membranes made with a polymer solution containing only PES and NMP have a large amount of macrovoids initiating at the top surface of the membrane and the addition of PVP helps to suppress the formation of macrovoids without drastically affecting the thermodynamics of mixing [37,38]. This change moves the composition path from instantaneous to delayed demixing (due to increased viscosity) which results in a morphological change from macrovoids to a dense bicontinuous structure [3,39].

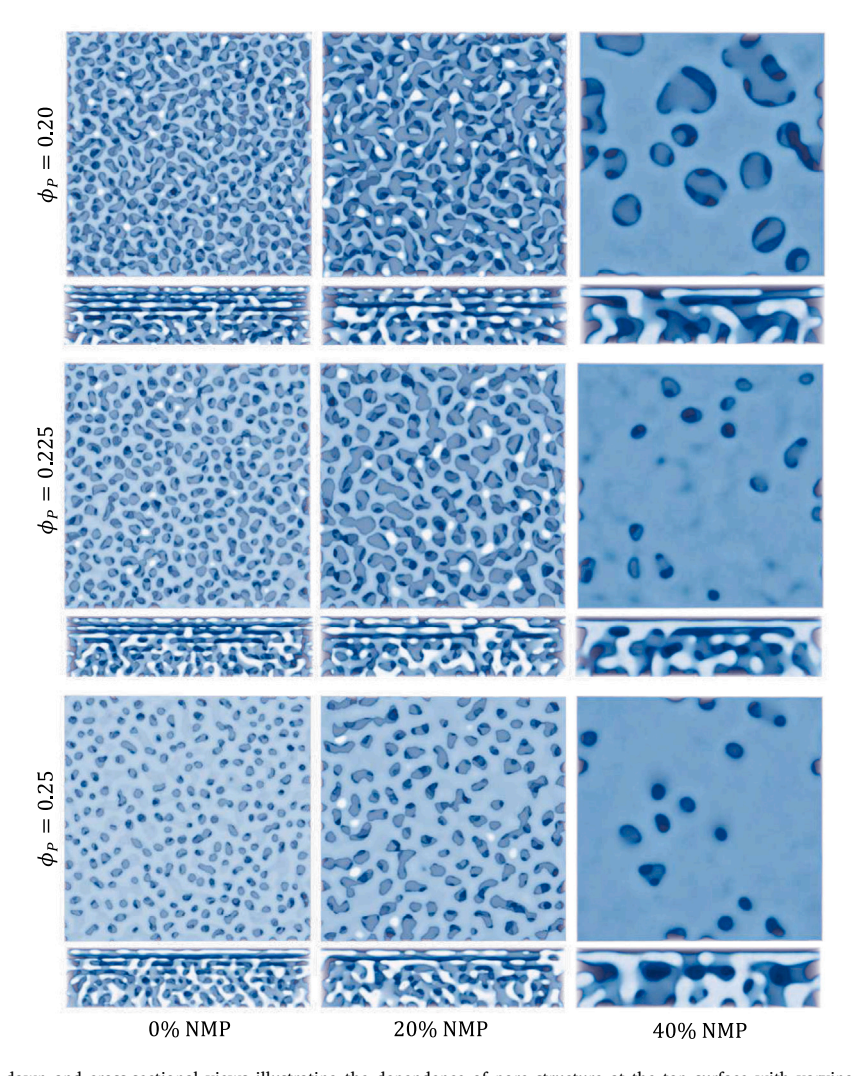


Fig. 10. 3D simulations with top-down and cross-sectional views illustrating the dependence of pore structure at the top surface with varying coagulation bath composition and polymer volume fraction. As NMP is added to the coagulation bath, the pore size at the top surface increases for each  $\bar{\phi}_P$  represented. As  $\bar{\phi}_P$  increases the pores decrease in size and the dense pore region fills in with more polymer.

# 3. Results & discussion

We performed simulations in both two and three dimensions to evaluate the effect of coagulation bath composition and polymer volume fraction on pore morphology. The two-dimensional simulations are clearly less computationally demanding, and this allowed us to extend the domain to greater depths thereby enabling better insight into the development of anisotropic pore structures. On the other hand, our 3D simulations were conducted with relatively shallower depths, but provided analysis of the top-surface pore morphology that is critical for membrane performance.

The domain size for the 2D simulations is  $8.96 \times 35.84~\mu m$  (resolved with a  $256 \times 1024$  grid). Hence, the depths of our 2D simulations closely correspond with the experimental membrane depth shown on the right side of Fig. 5. The domain size for the 3D simulations is  $8.96 \times 8.96 \times 2.24~\mu m$  (resolved with a  $256 \times 256 \times 64$  grid). We considered three different coagulation bath compositions:  $f_N^{CB}=1.0$ , 0.8, and 0.6, which represent adding NMP into the coagulation bath at 0 vol%, 20 vol%, and 40 vol%, respectively. In addition, three different polymer volume fractions were simulated:  $\bar{\phi}_P=0.2$ , 0.225, and 0.25. Hence, nine unique test cases were simulated in both 2D and 3D domains.

Our criterion for terminating a simulation was full vitrification throughout the domain. This criterion was met at different times for the three different coagulation bath compositions due to the fact that

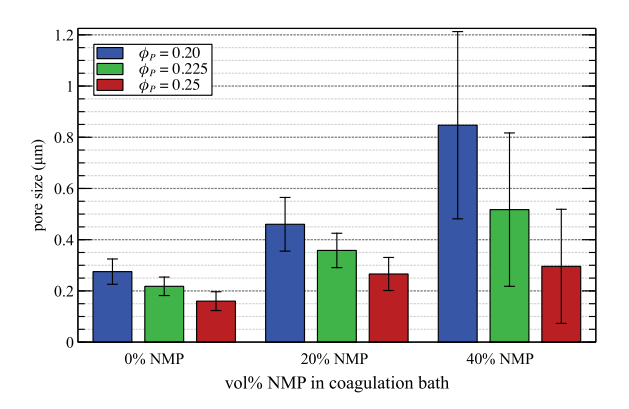


**Fig. 11.** Pore size at the membrane top surface versus coagulation bath composition for the three different polymer volume fractions. As NMP is added to the coagulation bath the pore size at the surface increases for each  $\bar{\phi}_P$  represented. As  $\bar{\phi}_P$  increases the pores decrease in size.

the  $f_N$  field evolves faster when its value at the top surface is higher. The two-dimensional simulations required 4.9s, 7.35s, and 9.8s to reach full vitrification for the three coagulation bath compositions  $f_N^{CB}=1.0$ , 0.8 and 0.6, respectively.

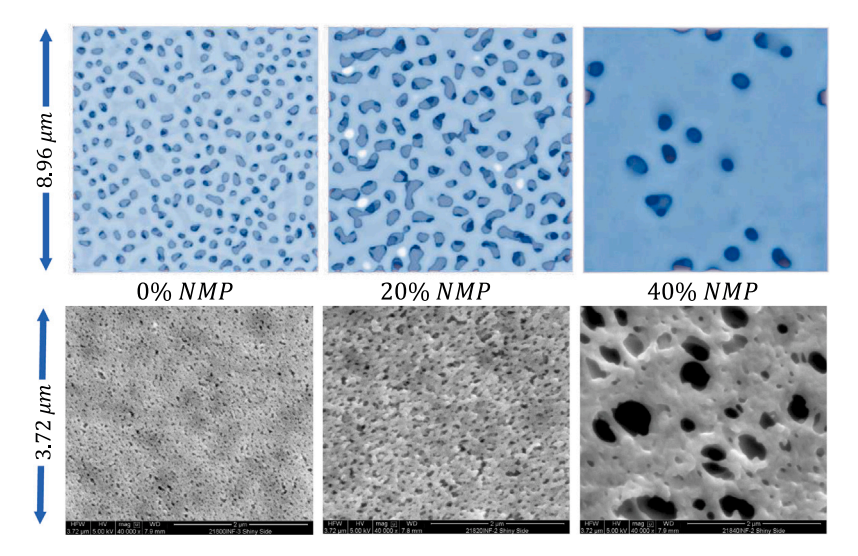


Fig. 12. Comparison of top surface pore morphology between experiments and simulations. From left to right the coagulation bath contained 0, 20, and 40 vol% NMP ( $f_N^{CB} = 1.0, 0.8$  and 0.6). The simulations here have a polymer volume fraction of  $\bar{\phi}_P = 0.25$ .

A comparison between the 2D simulations with a  $\bar{\phi}_P = 0.25$  and handcast membrane cross sections are seen in Fig. 6. The 2D simulations exhibit a dense pore region near the top surface where the non-solvent is in contact with the polymer solution. These initial pores develop quickly, as does vitrification, due to the early influx of nonsolvent into the polymer solution. At greater depths, whereby the in-flux of non-solvent is slower, larger pores are able to develop due to a slower nucleation process as well as a certain degree of phase coarsening that occurs. The addition of NMP to the coagulation bath (decreasing  $f_N^{CB}$  from 1.0 to 0.8 and 0.6) has a notable effect on morphology. When there is no NMP in the coagulation bath  $(f_N^{CB} =$ 1.0) very small pores rapidly form near the top surface of the domain resulting in a dense pore region. When 20 vol% NMP is added to the coagulation bath, the dense pore region near the top surface decreases in thickness and the entire domain exhibits larger pores. When 40 vol% NMP is added to the coagulation bath the most drastic difference is seen with the reduction in the dense pore region thickness and larger overall pore size.

In Fig. 7, we show a side-by-side comparison of the 2D pore morphologies for  $\bar{\phi}_P = 0.2$ , as well as a plot of the pore size versus membrane depth. In order to evaluate the pore size for the 2D simulations, each layer from top to bottom was scanned left to right and the average widths of the polymer-poor domains were computed (this was done via tracking the distance between phase interfaces). These widths were recorded as the pore size for that layer. To reduce noise, the pore depths were averaged within bins consisting of 31 layers, which are shown in Fig. 7. The plot quantitatively demonstrates that a higher amount of NMP in the coagulation bath results in a larger pore size. This trend is also seen with  $\bar{\phi}_P = 0.225$  and  $\bar{\phi}_P = 0.25$ , as shown in Figs. 8 and 9, respectively. In addition, it is found that the pore sizes decrease with increasing  $\bar{\phi}_P$ , which is expected. The porosity of the membranes at the end of the simulations correlates to the volume fraction of the polymer-rich phase, which can be calculated using a lever rule with a tie line extending from  $\phi_P = 0.0$  to  $\phi_P = \phi_{cutoff} =$ 0.75. The porosity for  $\bar{\phi}_P = 0.2$ , 0.225, and 0.25 is 0.73, 0.70, and 0.67 respectively.

The 3D simulations, with the dimensions given at the beginning of this section, were executed with the same conditions used in the 2D simulations described above. Due to the smaller depth, the 3D simulations required less physical time to reach full vitrification. The simulations were run for 0.1225s, 0.3575s, and 1.225s for coagulation bath compositions of  $f_N^{CB} = 1.0$ , 0.8, and 0.6 (0 vol% NMP, 20 vol% NMP, and 40 vol% NMP), respectively. The motivation for the 3D simulations was to analyze the pore morphology on the top surface

of the membrane, and how it depends on the physical conditions we varied. Supplemental Movies 2–5 provide animations of the 3D simulations.

Fig. 10 shows both top-down and cross-sectional views of the pore morphology for the nine unique conditions tested. The general trends found in the 2D simulations carry over to the 3D simulations, namely that pore size generally increases with increasing NMP content in the coagulation bath and decreasing polymer volume fraction. However, the 3D simulations also reveal distinct characteristics of the pore morphology at the top surface. In particular, we observe pore structures on the top surface that are continuous in some cases and discrete in other cases. For example, with  $\bar{\phi}_P=0.2$ , the pore structure is continuous along the top surface with 0% NMP in the coagulation bath, but transitions to a discrete pore structure with 40% NMP in the coagulation bath. In addition, when the coagulation bath composition is fixed at 0% NMP, the pore structure changes from continuous to discrete when the polymer volume fraction increases from  $\bar{\phi}_P=0.2$  to  $\bar{\phi}_P=0.25$ .

The quantitative values for pore size on the top surface from the 3D simulations are shown in Fig. 11. These pore size values were computed by scanning along two planes within the top layer of the membrane structure. The calculation is similar to that for the 2D simulations, however for each xy-plane a scan was conducted along the x-direction for each y-value. This provided more data, for which the average and the standard deviation (error bars) are shown in Fig. 11. Again, consistent with the 2D results, the pore size increases for all  $\bar{\phi}_P$  when NMP is added to the coagulation bath.

A comparison of the top-surface pore morphology between the experiments and the 3D simulations is given in Fig. 12. The pore size increases as NMP is added to the coagulation bath for both the experiments and simulations. The most drastic difference in morphology occurs when the coagulation bath contains 40 vol% NMP. In general, we find that the pore sizes for the top surface are larger in the simulations by approximately a factor of two to four when compared with experiments (see Figs. 11 and 12). The model does not accurately capture the smallest pores that form in the dense pore region near the top surface of the membranes as seen Fig. 6. We attribute this discrepancy to the length- and time-scale resolution of the simulations. Initial phase separation at the top surface occurs rapidly and would require a smaller grid spacing and time step to resolve the smaller pore sizes present in the experiments. The simulations in this work provide guidance for future studies by identifying the process conditions that warrant higher-resolution PF simulations to better study the top-surface morphology.

#### 4. Conclusion

The model presented here yields qualitative and quantitative insight to how different casting parameters can affect the pore size, anisotropic pore morphology, and surface pore size for membrane filters casted with PES/NMP/ Water. Two-dimensional simulations show that adding NMP to the coagulation bath decreased the thickness of the dense pore region near the top surface and increased the overall pore size throughout the cross section. Three-dimensional simulations show a significant variability of pore size in the top membrane surface with surface pores increasing in size with the addition of NMP into the coagulation bath. The top surface also exhibited a transition from continuous to discrete morphology as  $\bar{\phi}_P$  increased from 0.2 to 0.25. As expected both two- and three-dimensional simulations show that pore size decreases as polymer concentration increases. Comparisons drawn from handcast membranes showed similar trends, namely larger surface pores and a decrease in the dense pore region near the top surface when NMP is added to the coagulation bath. The pore sizes in the dense pore region near the top surface observed in experiments are smaller in size compared to the simulations. This discrepancy in size is attributed to the rapid formation of these regions where the coagulation bath comes into contact with the polymer solution. To fully resolve these differences a reduction in the time step size and grid spacing is required, which we leave for future work.

## CRediT authorship contribution statement

M. Rosario Cervellere: Conceptualization, Methodology, Software, Formal analysis, Writing - original draft. Xianghong Qian: Methodology, Writing - review & editing, Funding acquisition, Project administration. David M. Ford: Methodology, Writing - review & editing, Funding acquisition, Project administration. Christina Carbrello: Supervision, Resources, Project management, Writing - review & editing. Sal Giglia: Supervision, Resources, Project management, Writing - review & editing. Paul C. Millett: Conceptualization, Methodology, Software, Formal analysis, Supervision, Writing - original draft, Writing - review & editing, Funding acquisition.

# Declaration of competing interest

The authors declare that they have no known competing financial interests or personal relationships that could have appeared to influence the work reported in this paper.

## Acknowledgments

The authors would like to acknowledge funding from the MAST Center (Membrane Research Science and Technology Center) through NSF (Project no. IPP 1361809). The authors would like to acknowledge funding from the INTERN program in collaboration with Millipore-Sigma. The authors would also like to acknowledge the Arkansas High Performance Computing Center for the computational resources. The authors would like to acknowledge Susan Connolly and David Bell at MilliporeSigma for imaging membrane samples. The authors would like to acknowledge mentors from MilliporeSigma, 3M, and the MAST Center for guidance and insight to the direction of the project.

# Appendix A. Supplementary data

Supplementary material related to this article can be found online at https://doi.org/10.1016/j.memsci.2020.118779.

#### References

- [1] P. van de Witte, P. Dijkstra, J. van den Berg, J. Feijen, Phase separation processes in polymer solutions in relation to membrane formation, J. Membr. Sci. 117 (1) (1996) 1–31.
- [2] G.R. Guillen, Y. Pan, M. Li, E.M.V. Hoek, Preparation and characterization of membranes formed by nonsolvent induced phase separation: A review, Ind. Eng. Chem. Res. 50 (2011) 3798–3817.
- [3] A.K. Holda, I.F. Vankelecom, Understanding and guiding the phase inversion process for synthesis of solvent resistant nanofiltration membranes, J. Appl. Polym. Sci. 132 (2015) 42130.
- [4] J.F. Kim, J.H. Kim, Y.M. Lee, E. Drioli, Thermally induced phase separation and electrospinning methods for emerging membrane applications: A review, AIChE J. 62 (2016) 461–490.
- [5] X. Wang, H. Qian, L. Chen, Z. Lu, A. Lin, Dissipative particle dynamics simulation on the polymer membrane formation by immersion precipitation, J. Membr. Sci. 311 (2008) 251–258.
- [6] Y. He, Y. Tang, X. Wang, Dissipative particle dynamics simulation on the membrane formation of polymer-diluent system via thermally induced phase separation, J. Membr. Sci. 368 (2011) 78–85.
- [7] Y. Tang, Y. He, X. Wang, Effect of adding a second diluent on the membrane formation of polymer/diluent system via thermally induced phase separation: Dissipative particle dynamics simulation and its experimental verification, J. Membr. Sci. 409–410 (2012) 164–172.
- [8] Y. Tang, Y. He, X. Wang, Three-dimensional analysis of membrane formation via thermally induced phase separation by dissipative particle dynamics simulation, J. Membr. Sci. 437 (2013) 40–48.
- [9] Y. Tang, Y. He, X. Wang, Investigation on the membrane formation process of polymer-diluent system via thermally induced phase separation accompanied with mass transfer across the interface. dissipative particle dynamics simulation and its experimental verification, J. Membr. Sci. 474 (2015) 196–206.
- [10] Y. Tang, H. Lin, T. Liu, H. Matsuyama, X. Wang, Multiscale simulation on the membrane formation process via thermally induced phase separation accompanied with heat transfer, J. Membr. Sci. 515 (2016) 258–267.
- [11] H. han Lin, Y.-H. Tang, H. Matsuyama, X.-L. Wang, Dissipative particle dynamics simulation on the membrane formation of polymer-solvent system via nonsolvent induced phase separation, J. Membr. Sci. 548 (2018) 288–297.
- [12] G. Caneba, D. Soong, Polymer membrane formation through the thermalinversion process. 2. Mathematical modeling of membrane structure formation, Macromolecules 18 (1985) 2545–2555.
- [13] B. Barton, A. McHugh, Kinetics of thermally induced phase separation in ternary polymer solutions. I. Modeling of phase separation dynamics, J. Polym. Sci. B 37 (1999) 1449–1460.
- [14] B. Barton, A. McHugh, Modeling the dynamics of membrane structure formation in quenched polymer solutions. J. Membr. Sci. 166 (2000) 119–125.
- [15] G. Fernandes, J. Pinto, R. Nobrega, Modeling and simulation of the phaseinversion process during membrane preparation, J. Appl. Polym. Sci. 82 (2001) 3036–3051.
- [16] B. Zhou, A. Powell, Phase field simulations of early stage structure formation during imersion precipitation of polymeric membranes in 2D and 3D, J. Membr. Sci. 268 (2006) 150–164.
- [17] M. Hopp-Hirschler, U. Nieken, Modeling of pore formation in phase inversion processes: model and numerical results, J. Membr. Sci. 564 (2018) 820–831.
- [18] D. Tree, K. Delaney, H. Ceniceros, T. Iwama, G. Fredrickson, A multi-fluid model for microstructure formation in polymer membranes, Soft Matter 13 (2017) 3013–3030.
- [19] D. Tree, T. Iwama, K. Delaney, J. Lee, G. Fredrickson, Marangoni flows during nonsolvent induced phase separation, ACS Macro Lett. 7 (2018) 582–586.
- [20] D. Tree, L.D. Santos, C. Wilson, T. Scott, J. Garcia, G. Fredrickson, Mass-transfer driven spinodal decomposition in a ternary polymer solution, Soft Matter 15 (2010) 4614 4639.
- [21] Y. Mino, T. Ishigami, Y. Kagawa, H. Matsuyama, Three-dimensional phase-field simulations of membrane porous structure formation by thermally induced phase separation in polymer solutions, J. Membr. Sci 483 (2015) 104–111.
- [22] M.R. Cervellere, Y.-H. Tang, X. Qian, D.M. Ford, P.C. Millett, Mesoscopic simulations of thermally-induced phase separation in PVDF/DPC solution, J. Membr. Sci. 577 (2019) 266–273.
- [23] A. Akthakul, C. Scott, A. Mayes, A. Wagner, Lattice boltzmann simulations of asymmetric membrane formation by immersion precipitation, J. Membr. Sci. 249 (2005) 213–226.
- [24] Y. Gan, A. Xu, G. Zhang, Y. Li, H. Li, Phase separation in thermal systems: A Lattice Goltzmann study and morphoogical characterization, Phys. Rev. E. 84 (2011) 046715.
- [25] Y. Gan, A. Xu, G. Zhang, P. Zhang, Y. Li, Lattice Boltzmann study of thermal phase separation: Effects of heat conduction, viscosity and Prandlt number, Europhys. Lett. 97 (2012) 44002.
- [26] Y. Gan, A. Xu, G. Zhang, S. Succi, Discrete Boltzmann modeling of multiphase flows: hydrodynamic and thermodynamic non-equilibrium effects, Soft Matter 11 (2015) 5336–5345.

- [27] X. He, C. Chen, Z. Jiang, Y. Su, Computer simulation of formation of polymeric ultrafiltration membrane via immersion precipitation, J. Membr. Sci. 371 (2011) 108–116
- [28] J. Cahn, J. Hilliard, Free energy of a nonuniform system. I. Interfacial free energy, J. Chem. Phys. 20 (1958) 256–267.
- [29] P. Flory, Principles of Polymer Chemistry, Cornell University Press, 1971.
- [30] G. Tkacik, L. Zeman, Component mobility analysis in the membrane forming system water/N-methyl-2-pyrrolidone/polyethersulfone, J. Membr. Sci. 31 (1987) 273–288.
- [31] L. Zeman, G. Tkacik, Thermodynamic analysis of a membrane-forming system water/N-methyl-2-pyrrolodone/polyethersulfone, J. Membr. Sci. 36 (1988) 119-140
- [32] L. Xu, F. Qui, Simultaneous determination of three FloryeHuggins interaction parameters in polymer/solvent/nonsolvent systems by viscosity and cloud point measurements, Polymer 55 (2014) 6795–6802.
- [33] G. Phillies, Universal scaling equation fro self-diffusion by macromolecules in solution, Macromolecules 19 (1986) 2367–2376.

- [34] G. Phillies, The hydrodynamic scaling model for polymer self-diffusion, J. Phys. Chem. 93 (1989) 5029–5039.
- [35] F. Althena, J. Smid, J.V. den Berg, J. Wijmans, C. Smoulders, Diiffusion of solvent form a cast cellulose acetate solution during the formation of skinned membranes, Polymer 26 (10) (1985) 1531–1538.
- [36] J. Kim, Y. Kim, T. Kanamori, H. Lee, S. Kim, Vitrification phenomena in polysulfone/NMP/water system, J. Appl. Polym. Sci. 71 (1999) 431–438.
- [37] J.R. Hwang, S.-H. Koo, J.-H. Kim, A. Higuchi, T.-M. Tak, Effects of casting solution composition on performance of poly(ether sulfone) membrane, J. Appl. Polym. Sci. 60 (1996) 1343–1348.
- [38] S.H. Yoo, J.H. Kim, J.Y. Jho, J. Won, Y.S. Kang, Influence of the addition of PVP on the morphology of asymmetric polyimide phase inversion membranes: efect of PVP molecular weight, J. Membr. Sci. 236 (2004) 203–207.
- [39] M. Amirilargani, E. Saljoughi, T. Mohammadi, M. Moghbeli, Effects of coagulation bath temperature and polvinylpyrrolidone content on flat sheet asymmetric polyethersulfone membranes, Polym. Eng. Sci. (2010) 885–893.